



HAL
open science

The intrinsic ellipticity of dwarf spheroidal galaxies: constraints from the Andromeda system

Jean-Baptiste Salomon, Rodrigo Ibata, Nicolas Martin, Benoit Famaey

► To cite this version:

Jean-Baptiste Salomon, Rodrigo Ibata, Nicolas Martin, Benoit Famaey. The intrinsic ellipticity of dwarf spheroidal galaxies: constraints from the Andromeda system. *Monthly Notices of the Royal Astronomical Society*, 2015, 450 (2), pp.1409-1419. 10.1093/mnras/stv741 . hal-04595202

HAL Id: hal-04595202

<https://hal.science/hal-04595202v1>

Submitted on 30 May 2024

HAL is a multi-disciplinary open access archive for the deposit and dissemination of scientific research documents, whether they are published or not. The documents may come from teaching and research institutions in France or abroad, or from public or private research centers.

L'archive ouverte pluridisciplinaire **HAL**, est destinée au dépôt et à la diffusion de documents scientifiques de niveau recherche, publiés ou non, émanant des établissements d'enseignement et de recherche français ou étrangers, des laboratoires publics ou privés.



The intrinsic ellipticity of dwarf spheroidal galaxies: constraints from the Andromeda system

J.-B. Salomon,[★] R. A. Ibata, N. F. Martin and B. Famaey

Observatoire astronomique de Strasbourg, Université de Strasbourg, CNRS, UMR 7550, 11 rue de l'Université, F-67000 Strasbourg, France

Accepted 2015 March 31. Received 2015 March 31; in original form 2015 January 20

ABSTRACT

We present a study of the intrinsic deprojected ellipticity distribution of the satellite dwarf galaxies of the Andromeda galaxy, assuming that their visible components have a prolate shape, which is a natural outcome of simulations. Different possibilities for the orientation of the major axis of the prolate dwarf galaxies are tested, pointing either as close as possible to the radial direction towards the centre of Andromeda, or tangential to the radial direction, or with a random angle in the plane that contains the major axis and the observer. We find that the mean intrinsic axis ratio is $\sim 1/2$, with small differences depending on the assumed orientation of the population. Our deprojections also suggest that a significant fraction of the satellites, ~ 10 per cent, are tidally disrupted remnants. We find that there is no evidence of any obvious difference in the morphology and major axis orientation between satellites that belong to the vast thin plane of corotating galaxies around Andromeda and those that do not belong to this structure.

Key words: galaxies: dwarf – Local Group.

1 INTRODUCTION

The Local Group can be thought of as the closest laboratory for testing cosmological predictions on small scales, including the dynamical formation and evolutionary history of galaxies (Freeman & Bland-Hawthorn 2002). In this context the dwarf spheroidal (dSph) galaxies are of particular interest, as they represent the smallest of galactic systems, and are thought to be embedded in primordial dark matter subhaloes, thus giving us insights on the earliest epochs of galaxy formation in the Universe. The investigation of these satellites is thus one of the most active areas of Local Group research at present (Tolstoy, Hill & Tosi 2009). Their morphological parameters, their masses, their spatial distribution around their host, or the number of observed satellites, can be confronted with predictions of the Λ cold dark matter (Λ CDM) model (Kravtsov, Gnedin & Klypin 2004; Tollerud, Boylan-Kolchin & Bullock 2014). For example, their spatial distribution can provide insights on the shape of the dark matter halo of the host galaxy (Peñarrubia, Kroupa & Boily 2002), whilst the dwarf galaxies morphological characteristics can provide insights on their formation history (Zolotov, Hogg & Willman 2011; Carraro 2014).

The very nature of the dSphs as faint, poorly populated systems, poses several observational challenges, even for their identification in the Local Group. Generally, they have been discovered through the identification of small overdensities of stars over the contami-

nating foreground stellar populations (and background population of mis-identified compact galaxies). Improvements in instrumentation and analysis techniques have led to the discovery of several new Local Group dSph galaxies in recent years (Belokurov et al. 2006; Zucker et al. 2006; Walsh, Jerjen & Willman 2007; McConnachie et al. 2008; Martin et al. 2009, 2013). The known population of dSphs in the Local Group has thereby increased considerably (McConnachie 2012), which is now beginning to allow us to draw statistically firm conclusions about the properties of the dSph population. For instance, a recent discovery has shown that half of the dwarf galaxy satellites of the Andromeda galaxy (M31) reside in a vast thin plane around their host (VTP), and appear to have coherent motions (Ibata et al. 2013). This observational dynamical alignment is still not fully understood within the Λ CDM framework where the subhaloes that might host dSphs are a priori expected to possess only a weak alignment (Shaya & Tully 2013; Bahl & Baumgardt 2014; Ibata et al. 2014b; Pawlowski et al. 2014). Finding whether the satellites that partake in the alignment have a particular intrinsic shape and orientation that distinguishes them from the other dSphs orbiting around M31 may help in assessing whether the two sub-populations have experienced a different dynamical history.

The morphological properties of satellite dwarf galaxies can also provide tests of theoretical frameworks of galaxy formation on small scales. These galaxies are usually described as a baryonic component embedded in a massive dark matter halo (Walker et al. 2009), meaning that their stars are relatively protected from the tidal field of their giant host. But the formation of a plane of satellites (as

[★] E-mail: jean-baptiste.salomon@astro.unistra.fr

apparently required in M31), or any past interactions could have produced strong tidal effects that could have strongly affected their baryonic distribution and make them partly lose their dark matter halo. Another possibility is that some dSphs galaxies are actually not embedded in dark matter haloes at all, but are rather remnants of so-called tidal dwarf galaxies (TDG) which would have been created in an encounter between two major galaxies in the distant past, a scenario which might explain the formation of thin planes of galaxies such as the one observed around Andromeda (Pawlowski, Kroupa & de Boer 2011; Hammer et al. 2013) and around the Milky Way (e.g. Kroupa, Theis & Boily 2005; Kroupa et al. 2010; Pawlowski, Pflamm-Altenburg & Kroupa 2012). Such TDG would be mostly devoid of dark matter (Kroupa 1997), and would presumably be much more prone to tidal deformation than those embedded in primordial dark matter haloes. Some of the problems of this picture are in principle alleviated if the Modified Newtonian Dynamics framework (Milgrom 1983; Famaey & McGaugh 2012; Zhao et al. 2013) is adopted (Kroupa et al. 2010; Pawlowski & McGaugh 2014). Some other solutions consider the possibility of dissipative dark matter, as for example, in Foot & Silagadze (2013) or in Randall & Scholtz (2014).

In cosmological simulations, subhaloes are generally rounder than the host haloes. Subhaloes that have masses that are large enough to host dwarf galaxies have axis ratios : $0.65 \leq c/a \sim b/a \leq 0.95$ (Vera-Ciro et al. 2014). Observed dSphs are observed to be approximately roughly round: for the Milky Way, $\epsilon = 1 - a/b \sim 0.3$ (Martin, de Jong & Rix 2008). But we know that this observed ellipticity is just a projected view, and the third dimension could thus hide more elongated shapes. However, deprojecting to recover the intrinsic ellipticity is a challenge because distance uncertainties to different sides of the same dSph are currently far too large to allow any differential depth measurement except maybe in the Magellanic Clouds (Klein et al. 2014; Moretti et al. 2014). Therefore, in this paper, we propose a method which allows us to probe the third dimension, and we focus ourselves on M31.¹

In Section 2, we summarize the general method employed in this contribution, justify our hypotheses and present our data. Section 3 presents all dwarf galaxies parameters used in the analysis, which have been extracted from the observations. In Section 4, we define how our deprojection procedure is built. Results are then discussed in Sections 5 and 6, and our conclusions are drawn in Section 7.

2 METHOD

2.1 Hypotheses

In order to deproject the view and try to see which intrinsic ellipticity distribution can fit the observed projected distribution of stellar populations in the target dwarf, some simplifying hypotheses need to be made. In the following, two main hypotheses are adopted. First, we consider that dSphs have a prolate shape, like a cigar. This is indeed the natural shape of dark matter haloes in the relevant mass range (Vera-Ciro et al. 2014; Barber et al. 2015). In simulations, in which dwarf satellite galaxies are initially made of rotating stellar discs, this is a less natural assumption, but they can in principle also be deformed into a prolate shape through bar-like instabilities caused by ongoing small tidal interactions with the host (Łokas et al. 2010). Our second assumption will be to take an orientation of the

prolate body that is consistent with the observed projection of the major axis, as sketched in Fig. 1. Three cases will be considered:

- (i) the prolate dwarf galaxy is oriented perpendicular to the radial vector linking the host and the satellite,
- (ii) the major axis of the prolate dwarf galaxy is oriented as close as possible to the radial vector,
- (iii) the prolate dwarf galaxy has a random orientation that is consistent with the observed projection.

2.2 Data

In the present contribution, we will examine the structural properties of the dwarf galaxies surrounding the Andromeda galaxy (M31). Our observational data are derived from the Pan-Andromeda Archaeological Survey (PAndAS; McConnachie et al. 2009). This photometric survey with the MegaCam camera on the Canada–France–Hawaii Telescope has mapped a large area around Andromeda ($\approx 400 \text{ deg}^2$), allowing the discovery and characterization of the dwarf satellite galaxies of M31. A detailed account of the processing of the PAndAS survey through to the final catalogue of aperture magnitudes is given in Ibata et al. (2014a).

The PAndAS photometry was also used to estimate the distances to the dwarf galaxies, using the tip of the red giant branch method (Conn et al. 2012). By using a Markov Chain Monte Carlo (MCMC) approach that incorporated Bayesian priors on the expected morphology of the satellites and their luminosity function, Conn et al. (2012) were able to derive a posterior probability distribution function (PDF) for the distance to each of the satellites present in the survey.

From the homogeneous PAndAS data set, we also inferred the morphological parameters of all dwarf galaxies that fall in the survey footprint. These were derived using a version of the Martin et al. (2008) algorithm, updated for a full MCMC treatment, and which will be presented in another publication that is to be submitted soon (Martin et al., in preparation).

3 EXTRACTING DWARF GALAXY CHARACTERISTICS FROM THE OBSERVATIONS

3.1 Morphology and selection

The code developed by Martin et al. (2008) infers the following observational parameters: the projected ellipticity (ϵ , with $\epsilon = 1 - (a/b)$ where a is the minor axis of the adjusted ellipse and b the semimajor axis), the position angle (PA, the angle between the equatorial north and the major axis), and the half-light radius (r_h , taken along the major axis). The code was run on 23 dwarf galaxies present in the PAndAS survey and outputs posterior PDFs in the form of MCMC chains. We have also included in our study the dwarf elliptical satellites, NGC 147 and NGC 185. For them, realistic MCMC chains have been created by simultaneous drawings from Gaussian PDFs built from Crnojević et al. (2014), also derived from the PAndAS survey. According to Ibata et al. (2013), among these 25 satellites, 14 are in the VTP: And I, And III, And IX, And XI, And XII, And XIII, And XIV, And XVI, And XVII, And XXV, And XXVI, Cass II, NGC 147 and NGC 185. Whereas 11 are outside the VTP: And II, And V, And X, And XV, And XVIII, And XIX, And XX, And XXI, And XXII, And XXIII and And XXIV.

¹ The method presented here could be modified later on to be applied to dwarf satellites of the Milky Way.

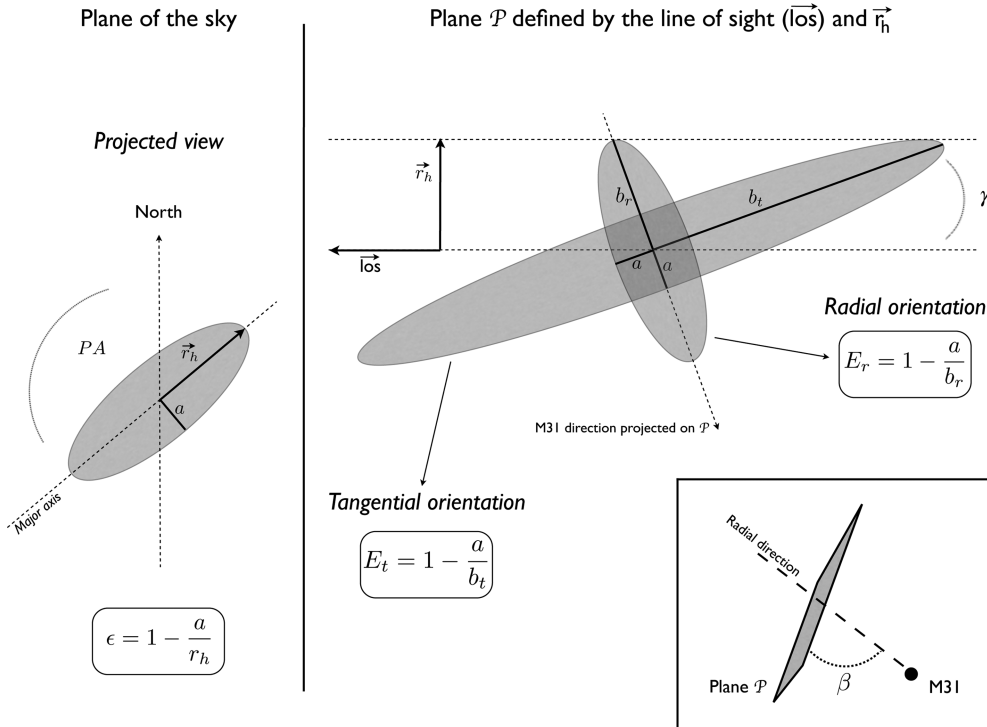


Figure 1. Sketch of the geometry. The left-hand panel shows the projected view on the sky, while the right-hand panel shows the view in the plane \mathcal{P} defined by the line of sight and the projected semimajor axis. Two cases are represented : the tangential case and the radial one. The bottom right-hand panel shows the position of the plane \mathcal{P} compared to M31, where β is the minimum angle between the radial direction and \mathcal{P} . The variable a is the semiminor axis of the prolate ellipsoid, equal to the semiminor axis of the projected ellipse. On the left-hand panel, PA is the angle between north and the semimajor axis \vec{r}_h where $||\vec{r}_h||$ is the observed half-light radius. On the right-hand panel, b_r is the intrinsic semimajor axis of the prolate ellipsoid placed in the configuration that is most radially-oriented with respect to M31, and b_t is the one placed in the tangential configuration. The line-of-sight position vector \vec{los} links the Earth to the centre of the satellites galaxy. The variable γ is the angle between the intrinsic major axis of the prolate ellipsoid and the line-of-sight position vector.

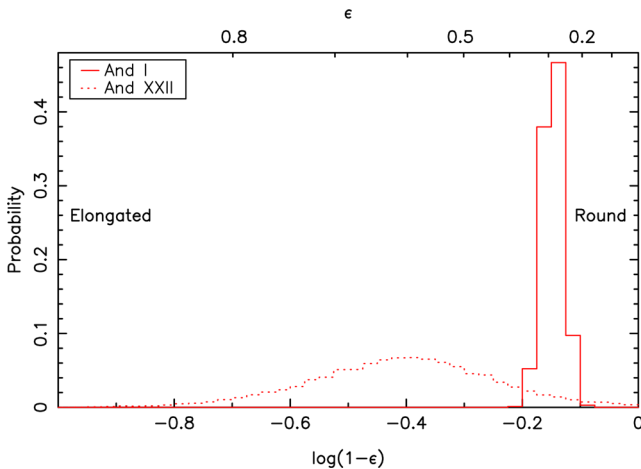


Figure 2. Representative projected ellipticity distributions. Histogram of the projected ellipticity for And I (solid line) and And XXII (dotted line) (two representative dSph in the sample) obtained from 10^5 draws from the Markov chain of Martin et al. (2008).

Thus, for each satellite k of Andromeda, the code provides us with a Markov chain that contains at each step i the positional and morphological parameters of interest: ϵ_{ki} , PA_{ki} and r_{hki} . For example, in Fig. 2 we display the PDF derived from 10^5 draws (this is typically the number of draws in all MCMC chains used in this study) of the projected ellipticity from the Markov chain of Andromeda I, an example of a rather round dSph galaxy with a large number of

resolved red giant stars and Andromeda XXII, an example of an extended dSph galaxy with a small number of resolved red giant stars. It is more representative to plot $\log(1 - \epsilon) = \log(a/b)$ where 0 corresponds to a round object.

When the whole sample of dSphs considered is taken into account, one draw from their respective Markov chain of ellipticity and distance represents a possible view from the Earth of the system of satellites around Andromeda. Fig. 3 represents the normalized average of the projected ellipticity of the satellites according to the derived PDFs for 10^5 random realizations (of the 25 satellites). Bins have been chosen to be large enough, $\log(1 - \epsilon) = 0.2$, to ensure reliable statistics. The vertical bars are 1σ standard deviations of the number of satellites per bin, derived from 7×10^4 draws.

As expected, the projected ellipticity shows predominantly round objects. Moreover, no significant difference between galaxies in the VTP (blue triangles) or outside it (grey squares) is evident.

3.2 Position in three dimensions

Once morphological parameters have been obtained, the position of each dSph centre in three dimensions has to be found. For that purpose, Andromeda's satellite galactic coordinates (α_k , δ_k) are considered perfect. We have chosen to take them from the literature in Collins et al. (2013) for Cassiopeia II and in McConnachie (2012) for the other ones. For the third dimension, the distance from Earth (d), we use results found by Conn et al. (2012) (see Fig. 4). This provides us with a Markov chain of distance for each galaxy d_k . Each step i of it gives a possible d_{ki} for the satellite.

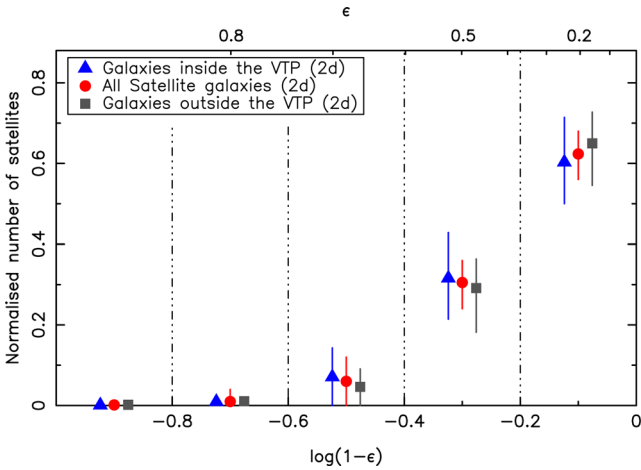


Figure 3. Observed (i.e. projected) ellipticity derived from the PAndAS survey, showing the average distribution of ellipticity for the 25 satellites, randomly drawn 10^5 times from each of the 25 Markov chains. Bin sizes are $\log(1 - \epsilon) = 0.2$. Red circles are the ellipticity distribution of the entire system of 25 dwarf galaxies. Blue triangles correspond to the 14 dwarf galaxies contained in the vast thin plane of satellites (Ibata et al. 2013), while the grey squares are for the 11 outside of the VTP. Vertical error bars indicate one standard deviation derived from this experiment.

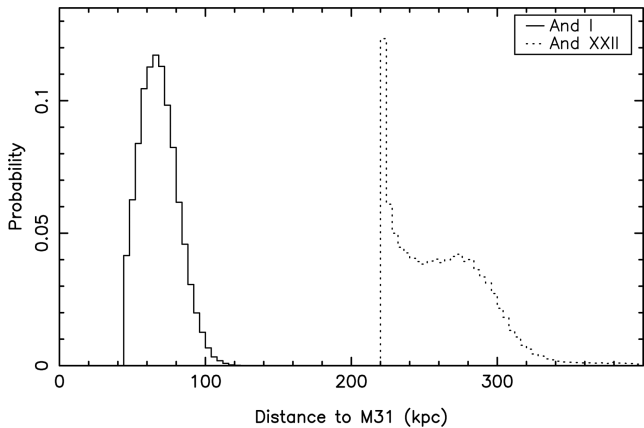


Figure 4. Histogram of the distance of the centre of two representative systems, And I (solid line) and And XXII (dotted line) from the centre of M31 (derived from 10^5 draws from the Markov chain of Conn et al. 2012).

For a dwarf galaxy, a drawing in its morphological Markov chain and one in its distance Markov chain combined with sky coordinates provide a set of six parameters. They define a possible representation in space of the centre around Andromeda in association with three possible projected morphological characteristics: α_k , δ_k , d_{ki} , ϵ_{ki} , PA_{ki} and r_{hki} .

3.3 Model

In all the following analysis, the intrinsic shape of the dwarf galaxies is approximated as a prolate ellipsoid, which is a natural outcome of dark matter satellites in Λ CDM simulations (Vera-Ciro et al. 2014; Barber et al. 2015). With this assumption the satellites have two equal minor axes (a) and one major axis (b). Consequently, since a prolate structure is symmetrical by rotation around the major axis, the projected minor axis remains identical, irrespective of the point of view. Thus, the apparent minor axis of the ellipse given by the

projected satellite is taken to measure the real minor axis (a). On the other hand, r_h is known, defined by PA and r_h .

Of course, due to the projection on the sky, the real major axis b is not equal to r_h : b can have any orientation in the plane (\mathcal{P}) defined by the line of sight and r_h (see Fig. 1). Thus, an additional condition is required to fix the three-dimensional orientation of the major axis, and consequently the intrinsic ellipticity of the satellites. We consider three possibilities which will be discussed in Section 4.

3.4 Limitation of the major axis

As defined above, the intrinsic major axis b has to lie in the plane \mathcal{P} . However, depending on the parameter set drawn from the chain, it is possible that b can take on physically implausible values. To avoid this situation, we implement a filter to reject solutions where b would be larger than the tidal radius of the satellite (tidal rejection criterion). Thus, the tidal radius is considered as the maximal radius:

$$b < \left(\frac{M_{\text{sat}}}{2M_{\text{host}}} \right)^{1/3} R, \quad (1)$$

where M_{sat} is the satellite mass and M_{host} the mass of the host galaxy contained in the sphere of radius R (distance between the satellite centre and the host galaxy centre). We estimate M_{host} using an NFW (Navarro, Frenk & White 1997) halo model (with virial mass $2 \times 10^{12} M_{\odot}$, a mean value of recent results (Watkins, Evans & An 2010; Fardal et al. 2013)). The value of M_{sat} is derived from the line-of-sight velocity dispersion (σ_v) listed in McConnachie (2012) for NGC 147 and NGC 185 and in Collins et al. (2013) for the other galaxies, taking

$$M_{\text{sat}} \sim \frac{\sigma_v^2 b}{G}, \quad (2)$$

where G is the gravitational constant. Consequently, with equations (1) and (2), the following limit can be set to b :

$$b < \sigma_v \sqrt{\frac{R^3}{2G M_{\text{host}}}}. \quad (3)$$

Given the large uncertainties in σ_v , we wish to remain conservative and so as not to eliminate physically possible cases, we adopt the values corresponding to the listed value of σ_v plus one standard deviation. In the following analysis, this criterion is always automatically applied, and it forces the rejection of approximately 5 per cent of the MCMC parameter trial values. Finally, to avoid the MCMC process from exploring unrealistic solutions, we limited the projected half-light radius to 20 arcmin.

3.5 Simple test

We constructed a simple toy model to test the algorithms that we developed and to obtain a first assessment of the magnitude of the effect of de-projection on the ellipticity distribution. Three-dimensional prolate dwarf galaxies are generated with a random size (in the range of the observed dwarf satellites galaxies) and are placed at random locations around the Andromeda galaxy (again in the observed range). In Fig. 5, we show the consequence of assuming that the intrinsic ellipticity is given by the observed *projected* distribution previously displayed in Fig. 3 (red dots). These prolate structures are observed from a position corresponding to Earth, and we measure the projected ellipticity that the artificial structures would then be seen to possess (purple triangles). As expected, the projected distribution will appear rounder than the

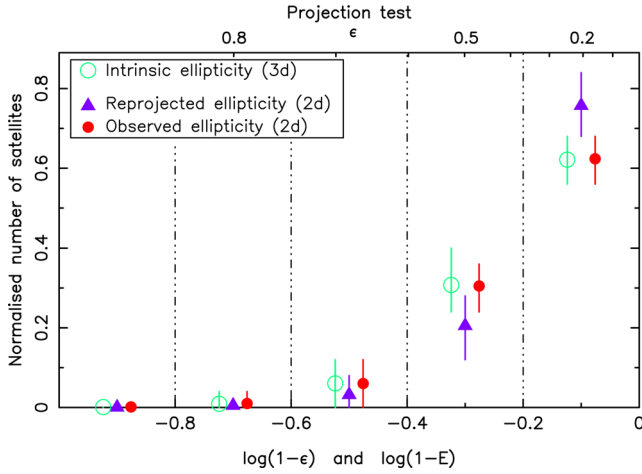


Figure 5. Green circles represent the intrinsic ellipticity chosen for this test. Purple triangles represent the distribution of projected ellipticity for 1000 three-dimensional systems of 25 dSph galaxies generated from a random distribution of position and from the green distribution for the ellipticity. Red dots are the observed ellipticities previously seen in Fig. 3. Vertical error bars indicate one standard deviation.

intrinsic distribution. The differences in the rounder bin is about 2σ , thus confirming that the projected distribution cannot be seen as the three-dimensional one.

4 DEPROJECTION

Our next task is to find the distribution of intrinsic ellipticities that is consistent with the observed projected distribution of Fig. 3, and with the observed orientations and distances of the real satellites. As stated above, this will require an additional geometric constraint, which we will implement via an assumption regarding the three-dimensional orientation of the satellites.

4.1 Tangential deprojection

As a first hypothesis, we suppose that each satellite is oriented tangentially with respect to the vector \mathbf{r}_s connecting it to M31, i.e. that the real semimajor axis (b) of the modelled dwarf galaxy is on the plane \mathcal{P}' perpendicular to \mathbf{r}_s . For satellite k , a given set i of parameters (l_k, b_k, d_{ki}) then uniquely defines the direction of the vector \mathbf{b} , which corresponds to the intersection of \mathcal{P} and \mathcal{P}' . Once the direction of \mathbf{b} is known, $\|\mathbf{b}\|$ is determined by requiring that it correspond to the projected view of the dwarf galaxy whose apparent semimajor axis is $\|\mathbf{r}_h\|$. Finally, the intrinsic ellipticity $E_{T_{ki}}$ assuming this ‘tangential hypothesis’, is calculated (see Fig. 6). In Appendix A, we describe this deprojection in more detail.

As the tangential deprojected chain of each of the dwarf galaxies is now known, a random draw from each of the Markov chains gives a system of satellites all of which are in tangential orientation. This procedure is repeated to obtain the global ellipticity distribution of the dwarf galaxy system, which is shown in Fig. 7. Under this ‘tangential’ assumption, the intrinsic distribution of ellipticity is substantially flatter than the projected ellipticity, and produces a long tail of highly flattened systems. No significant difference between galaxies within the VTP or outside of it is apparent.

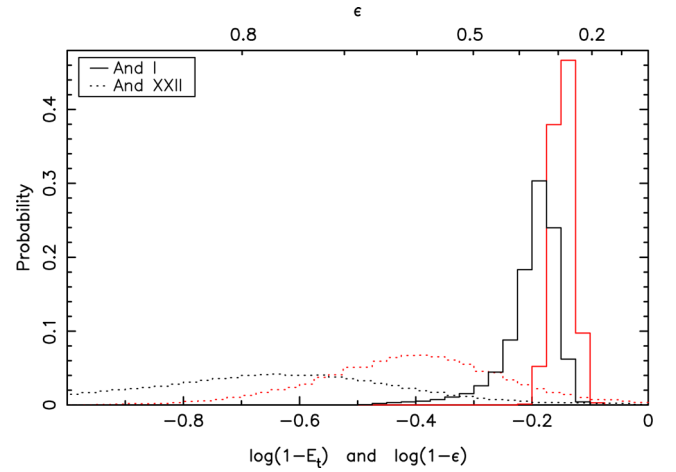


Figure 6. Histogram of the ellipticity for And I (solid black line) and And XXII (dotted black line) after tangential deprojection obtained from 10^5 draws of the MCMC chain. The red curves are the observed ellipticity previously seen in Fig. 2.

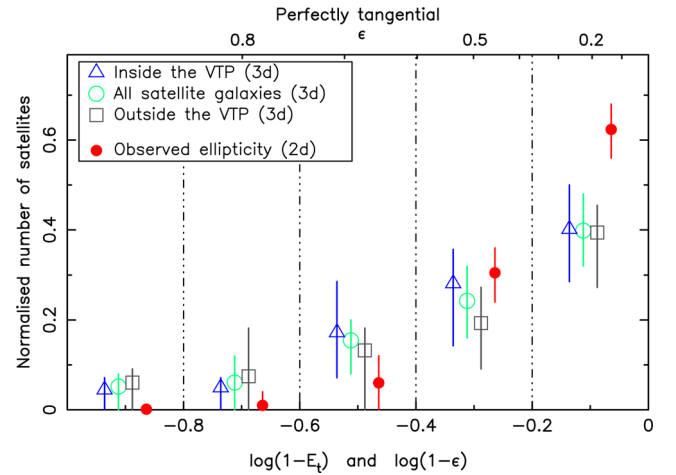


Figure 7. Distribution of tangentially deprojected ellipticity for 10^5 systems generated from Markov chains derived from the observational analysis. Green circles mark the ellipticity distribution of the entire system of 25 dwarf galaxies. Blue triangles are for those contained in the vast thin plane of galaxies (Ibata et al. 2013), 14 dSphs and grey squares are for those outside the VTP, 11 dSphs. Red dots are the observed ellipticities previously seen in Fig. 3. Vertical error bars indicate one standard deviation.

4.2 Radial deprojection

The second hypothesis that we explore in this analysis is to consider that the satellites are oriented as close as possible to the radial direction with respect to Andromeda. As before, the major axis \mathbf{b} must lie on \mathcal{P} . For this ‘radial’ deprojection, we would like \mathbf{b} to lie along \mathbf{r}_s . However, the prolate ellipsoid must also be consistent with the observed (projected) orientation of the galaxy. In this situation, we have three spatial unknowns that have to respect four independent equations, so that the problem turns out to be overconstrained. Thus, an exact radial orientation is, in general, impossible.

A way to resolve the problem is to attempt to orient the prolate ellipsoid as close as possible to a radial direction. To this end, we minimize the angle β , between \mathbf{r}_s and \mathbf{b} such that the projection of \mathbf{b} yields \mathbf{r}_h . Consequently, β is the minimum angle, an incompressible lower limit, that can exist between the radial vector and the major

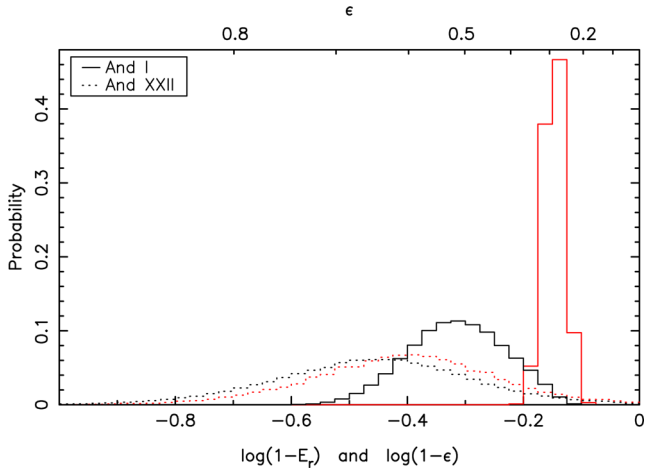


Figure 8. Histogram of the ellipticity for And I (solid black line) and And XXII (dotted black line) after radial deprojection obtained from 10^5 draws of the MCMC chain. The red curves are the observed ellipticity previously seen in Fig. 2.

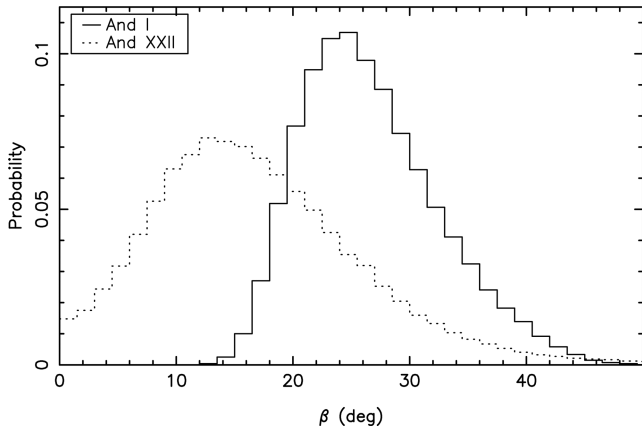


Figure 9. Probability density function of the angle β between the major axis of: And I (solid line), And XXII (dotted line) and their respective radial direction after radial deprojection (obtained from 10^5 MCMC draws).

axis vector of a dwarf galaxy according to our data. The intrinsic ellipticity (assuming this ‘radial’ hypothesis) $E_{R_{ki}}$ is thus obtained (see Fig. 8) coupled with β_{ki} (see Fig. 9). For more details, see Appendix B.

The radially deprojected ellipticity is displayed in Fig. 10, and interestingly, the roundest bin is not dominant, and a significant number of highly elliptical systems are required if this assumption is realistic. Again, differences between galaxies within the VTP of galaxies and outside of it are not significant.

4.3 γ -deprojection (random angle within \mathcal{P})

In the previous subsections, we considered a ‘tangential’ and a ‘radial’ deprojection. We have seen that a satellite can always be fit to a three-D tangential orientation, but that a prolate system cannot be placed closer to a radial direction than a minimum angle β (which depends on the structure and position of the satellite). However in reality, we do not have observational information that allows us to

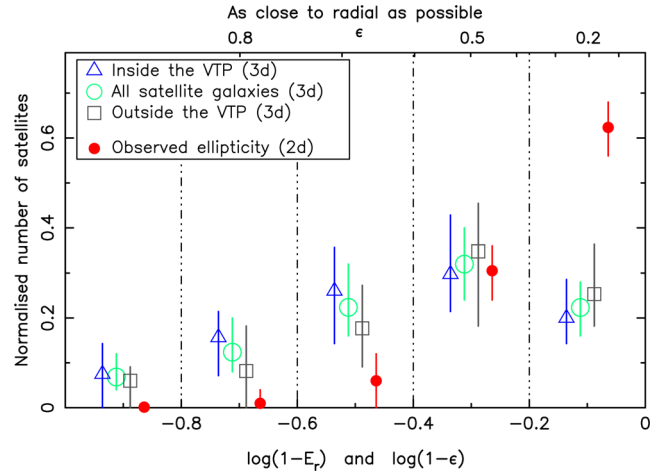


Figure 10. As Fig. 7, but for the radial deprojection method.

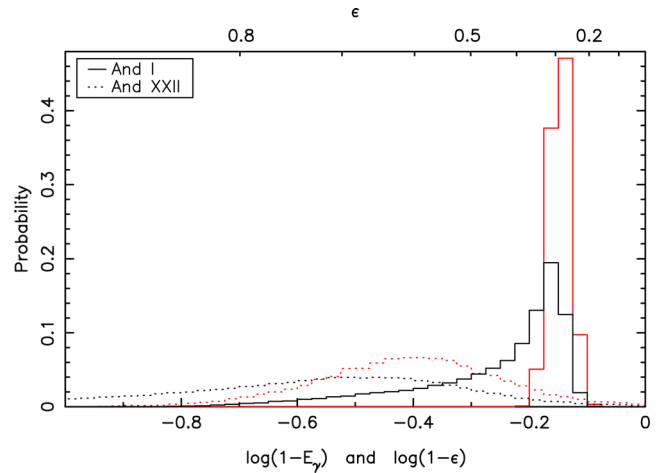


Figure 11. Histogram of the ellipticity for And I (solid black line) and And XXII (dotted black line) after γ -deprojection obtained from 10^5 draws of the MCMC chain. The red curves are the observed ellipticity previously seen in Fig. 2.

favour either of these orientations, and we only know that the major axis lies within the line-of-sight plane \mathcal{P} . This motivates our final deprojection, where we instead make the minimal assumption that the satellites are randomly oriented within \mathcal{P} . The random angle γ , is the angle between the line of sight and the major axis \mathbf{b} . The intrinsic ellipticity (assuming this ‘gamma’ hypothesis) $E_{\gamma_{ki}}$ is thus obtained (see Fig. 11) coupled with γ_{ki} (see Fig. 12).

The resulting deprojection is shown in Fig. 13 and presents a rather flat ellipticity distribution. Again, there is almost no difference between the dwarf galaxies that belong to the VTP and those outside of it.

5 RE-PROJECTION TESTS

The distributions of ellipticity obtained in Figs 7 and 10 take into account the observational information with a hypothesis on the orientation and on the prolate shape of the satellite galaxies. In contrast, the distributions of ellipticity obtained in Fig. 13 take into account the observational information assuming that the shape of the satellite galaxies is prolate, but that no particular direction can be privileged. If either of these approaches is realistic, one of

the resulting deprojected distributions should be the real intrinsic ellipticity.

To test the consistency of this approach, we decided to examine whether the derived deprojected ellipticity distributions would give rise to projected distributions similar to the observed distribution of ϵ for random viewing directions.

To this end, we modelled systems containing 25 (three-dimensional) prolate ellipsoids with random orientation. The ellipticity, and so the semimajor axis, is randomly picked from the 3D tangential-deprojected ellipticity distribution. The positions of the dwarf galaxy models are drawn randomly inside a sphere of 450 kpc around the host. A set of 1000 such systems were generated and observed from a position equivalent to that of the Earth point at 780 kpc from the host galaxy. The final 2D projected ellipticity is shown Fig. 14. The same test is applied with the 3D radial-deprojected ellipticity and the 3D γ -deprojected one. Results are shown in Figs 15 and 16, respectively.

In Fig. 15, one can see that the projected ellipticity distribution (purple triangles) based on the radial deprojection does not reproduce well the observed distribution of ellipticity (red circles) in the roundest bin. This means that if dwarf galaxies are prolate

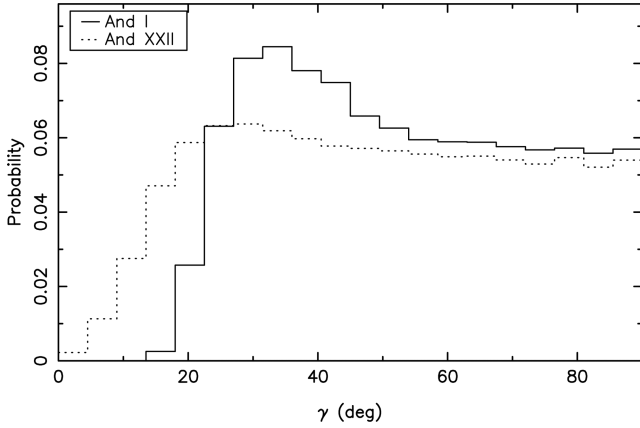


Figure 12. Probability density function of the angle γ (in degrees) between the major axis of And I (solid line) and And XXII (dotted line) with their respective radial direction after γ -deprojection (obtained from 10^5 MCMC draws).

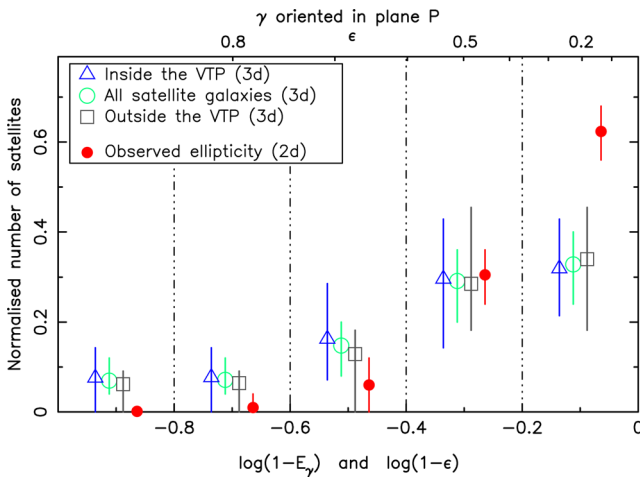


Figure 13. As Fig. 7, but for the γ deprojection method (where we assume that the major axis lies in plane \mathcal{P} at a random angle with respect to the line of sight).

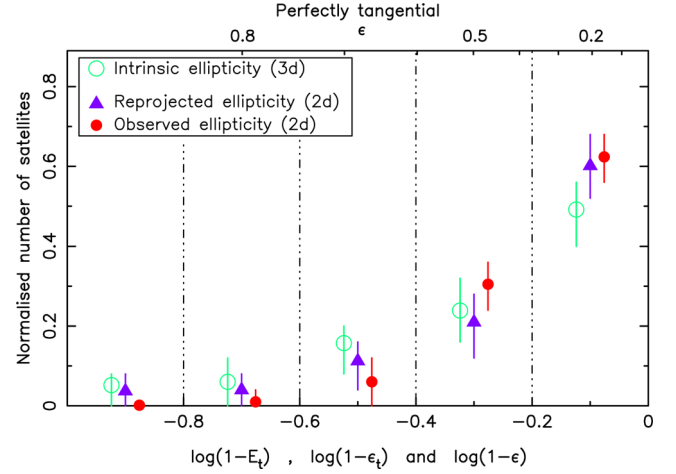


Figure 14. Distribution of projected ellipticity for 1000 sets of 25 *dSph* satellites randomly built with intrinsic ellipticity picked from the tangentially deprojected distribution (purple triangles). Red dots show the distribution of observed ellipticities. Green circles are the intrinsic ellipticity determined with the tangential deprojection method represented in Fig. 7. Vertical error bars indicate one standard deviation.

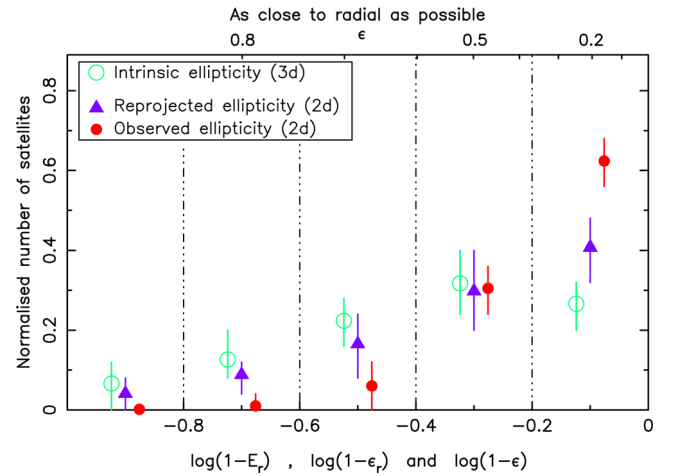


Figure 15. As Fig. 14, but for the radial deprojection method.

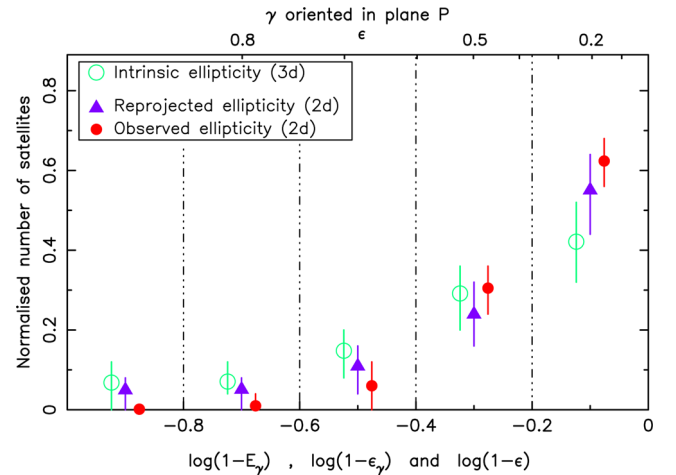


Figure 16. As Fig. 14, but for the γ -deprojection method.

structures, and if our viewing direction is not special, the galaxies are not oriented in a radial configuration. However, the projected distributions based on tangential (Fig. 14) or the γ (Fig. 16) methods are perfectly consistent with the observed distribution of ellipticity. We consider that this is a good consistency test of our method. Thus, modelling dwarf galaxies as possessing prolate shapes can give self-consistent solutions in terms of their derived ellipticity distribution. Furthermore, the population of dwarf galaxies around Andromeda can be considered as a drawing from a distribution of general intrinsic ellipticity.

6 INDIVIDUAL CASES AND DISCUSSION

The results for all of the dSph galaxies are listed in Table 1. The second column contains the character ‘p’ if the galaxy belongs to the VTP according to Ibata et al. (2013), and ‘a’ otherwise. Columns 3 and 4 contain the mean observed ellipticity and the mean observed half-light radius obtained with the method of Martin et al. (2008). Column 5 is the mean distance from M31 to the centre of the dSph galaxy obtained by Conn et al. (2012). Note that these observed average values (columns 3–5) take into account the fact that some values have been rejected by our tidal criterion in the γ -deprojection method. Columns 6, 8 and 10 represent the mean of the tangential-deprojected, radial-deprojected and γ -deprojected ellipticity obtained with our method. Columns 7, 9 and 11 are the percentage of excluded cases by our tidal criteria for the three deprojections. The last column is the angle β previously defined as the geometrically minimum possible angle between the radial direction and the plane \mathcal{P} . All uncertainties indicate one standard deviation of each parameter with our method.

First, the most powerful geometric constraint is a high angle β . Indeed, it corresponds to the lower limit for a radial orientation. This means that even if the orientation is unknown, a dwarf galaxy cannot be closer to the radial direction than β (see Fig. 1). This criterion does not depend at all on our hypothesis. Thus, in the present study, we have identified six dwarf galaxies – And II, And III, And XXI, And XXIII, CasII and NGC 147, which can absolutely not be radially oriented. For this we have chosen a criterion such that $\beta - 1\sigma > 25^\circ$ (where σ is here the standard deviation of β). These dwarf galaxies are relatively close to their host. Moreover, they mostly have a large half-light radius and favour a high ellipticity (more than 0.5) in each kind of deprojection. Also, for five of these six galaxies, the γ -deprojection shows the largest rate of tidal rejections among the three cases. These particularities suggest that these six dwarf galaxies may be largely affected by their environment and could be affected by tides or even remnants of ancient TDG. For the most massive object, NGC 147, This last result is in good agreement with Crnojević et al. (2014) where they have recently found that NGC 147 presents tidal tails. Moreover, it could also indicate that it is beginning to be stretched due to gravitational interactions, as attested by the stellar stream that emanates from it (McConnachie et al. 2009).

It is also interesting to see the deprojection behaviour of the other dwarf galaxies that have an observed large half-light radius and a high level of tidal rejections with all three deprojection methods. And XII, And XIX and And XXV are such cases. This might be due to the effects of tidal interactions with M31, as argued by Collins et al. (2014) for And XIX and And XXV (as well as And XXI). Moreover, this strongly suggests that these galaxies are close to being destroyed and becoming stellar streams. Please note that we have been conservative in estimating the tidal limits of the dwarf galaxies, as we used the measured velocity dispersion *plus* one

standard deviation to calculate the tidal limits. Thus, the percentage of tidal rejections listed in Table 1 should be considered as lower limits.

Finally, And XIII and And XXII have a large intrinsic ellipticity with all of the deprojection choices. Indeed, with the three deprojections, they always conserve an ellipticity around 0.7. Thus, these dSph galaxies are intrinsically very elongated.

As the re-projection tests suggest a possible tangential orientation being very plausible, we have examined in this case the deprojected ellipticity as a function of the distance (Fig. 17). Blue circles are the values for the satellites within the VTP and grey circles are the values for those outside. There is a priori no obvious correlation. Nevertheless, a close inspection of the repartition of the satellites outside of the VTP seems to indicate a relatively tight correlation between 100 and 200 kpc: dSphs are more elongated when closer to M31. No such correlation is present for satellites in the VTP. With the large error bars, no strong conclusion can be drawn, but it would be interesting to compare this with different models, both in standard cosmology in which the VTP could have been recently accreted and in alternative scenarios such as those based on TDGs.

We next examine the properties of the population of 25 dwarf galaxies as a whole, which we consider as a representative sample for this kind of object. The ellipticity of this group is listed in Table 2 for projected (ϵ), tangential-deprojected (E_t), radial-deprojected (E_r) and γ -deprojected (E_γ) with their total percentage of tidal rejection.

This percentage is compatible with a physical behaviour with a high value for tangential and γ deprojection and a much lower value for the radial deprojection. Objects in a radial configuration are falling towards their host with a compact shape whereas objects in tangential or random orientation are suspected to have been strongly disrupted in their orbits around their host.

As expected, each kind of deprojection gives a larger ellipticity (with a minimum of 0.44) than the projected observations. Thus, these dwarf galaxies tend to possess an elongated shape with a minor to major axis ratio (a/b) of approximately 1/2. Vera-Ciro et al. (2014) and Barber et al. (2015) find a slightly larger but coherent axis ratio in the inner regions (~ 1 kpc) of the dark matter satellites in the Aquarius simulation that could possibly host stars. Thus, our conclusion appears to be consistent with the possibility that stellar components in the Andromeda satellite galaxies possess the same shape. This is perhaps not incompatible either with them being remnants of ancient TDG. These observational values can in any case serve as a test of various models in the future.

7 CONCLUSIONS

First of all, we have seen that adopting a prolate shape for the dwarf satellite galaxies of Andromeda gives a coherent solution in the sense that the derived ellipticity distribution for the real viewing direction is similar to what would be derived from a random vantage point. This simplifying assumption has allowed us to derive the intrinsic ellipticity for the entire population of satellites. The resulting ellipticity distribution is found to be relatively flat between $\log(1 - \epsilon)$ of 0 to -0.4 before decaying at larger ellipticities. Some of the dwarf galaxies are found to be intrinsically significantly elongated. This is probably not incompatible with them being remnants of ancient TDG as recently found by, e.g. Yang et al. (2014), but it could also be consistent with dwarf galaxies having the same shape as their hosting dark matter subhalo. Secondly, no clear difference in ellipticity between the satellites inside the VTP and those outside of it was noticed. The two populations of galaxies seem to

Table 1. Properties of the 25 satellites of Andromeda studied here, showing the results of the three different deprojections obtained from 10^5 draws of the MCMC chain. (1) Ibata et al. (2013) (2) According to Cmojović et al. (2014) for NGC147 and NGC185 and to Martin et al. (in preparation) for the other galaxies (3) Conn et al. (2012).

Name	VTP (1)	ϵ (2)*	n_h (arcmin) (2)*	d_{M31} (kpc) (3)*	E_t	Tide (per cent)	E_r	Tide (per cent)	E_γ	Tide (per cent)	β (deg)
And I	p	0.29 ± 0.03	3.97 ± 0.14	68.7 ± 13.3	0.37 ± 0.05	1.8	0.51 ± 0.10	0.0	0.43 ± 0.15	14.3	26.7 ± 6.0
And II	a	0.14 ± 0.02	5.13 ± 0.10	197.0 ± 11.0	0.15 ± 0.02	0.0	0.57 ± 0.09	0.3	0.31 ± 0.20	5.0	43.4 ± 3.3
And III	p	0.59 ± 0.03	1.89 ± 0.15	91.2 ± 13.9	0.66 ± 0.05	0.4	0.76 ± 0.06	0.0	0.71 ± 0.13	6.8	40.9 ± 7.7
And V	a	0.28 ± 0.07	1.68 ± 0.14	116.3 ± 5.9	0.70 ± 0.15	7.9	0.31 ± 0.07	0.0	0.47 ± 0.22	3.3	16.2 ± 7.1
And IX	p	0.12 ± 0.07	1.85 ± 0.21	138.4 ± 52.3	0.12 ± 0.08	0.0	0.63 ± 0.23	6.5	0.29 ± 0.23	1.9	11.0 ± 7.2
And X	a	0.30 ± 0.18	1.15 ± 0.24	143.9 ± 27.6	0.36 ± 0.20	0.1	0.54 ± 0.19	0.4	0.47 ± 0.28	2.6	12.5 ± 8.9
And XI	p	0.24 ± 0.16	0.78 ± 0.20	141.0 ± 41.7	0.46 ± 0.31	2.6	0.41 ± 0.27	0.4	0.43 ± 0.29	1.3	34.4 ± 24.1
And XII	p	0.39 ± 0.25	2.85 ± 1.36	157.7 ± 52.2	0.47 ± 0.26	15.2	0.56 ± 0.24	5.1	0.50 ± 0.27	18.7	15.9 ± 12.9
And XIII	p	0.54 ± 0.16	1.11 ± 0.41	180.2 ± 81.2	0.71 ± 0.19	6.9	0.65 ± 0.17	0.0	0.68 ± 0.19	3.1	9.8 ± 7.4
And XIV	p	0.20 ± 0.11	1.55 ± 0.16	184.4 ± 34.9	0.58 ± 0.28	10.1	0.25 ± 0.13	0.0	0.39 ± 0.25	3.0	13.4 ± 10.4
And XV	a	0.24 ± 0.10	1.39 ± 0.13	167.9 ± 45.5	0.26 ± 0.10	0.4	0.73 ± 0.20	18.7	0.42 ± 0.24	3.5	36.2 ± 13.7
And XVI	p	0.29 ± 0.08	1.00 ± 0.08	316.1 ± 33.7	0.30 ± 0.08	0.0	0.79 ± 0.08	0.2	0.49 ± 0.23	0.7	21.9 ± 3.0
And XVII	p	0.42 ± 0.10	1.39 ± 0.21	71.8 ± 21.0	0.49 ± 0.12	7.4	0.66 ± 0.15	0.5	0.55 ± 0.16	13.8	30.5 ± 11.0
And XVIII	a	0.21 ± 0.13	0.78 ± 0.11	454.6 ± 40.1	0.22 ± 0.14	0.0	0.73 ± 0.14	0.4	0.40 ± 0.28	0.4	7.6 ± 4.8
And XIX	a	0.41 ± 0.09	11.65 ± 1.64	183.8 ± 55.2	0.49 ± 0.08	74.4	0.56 ± 0.17	65.2	0.49 ± 0.12	72.5	3.7 ± 2.7
And XX	a	0.30 ± 0.20	0.77 ± 0.25	141.7 ± 13.4	0.57 ± 0.31	2.9	0.38 ± 0.24	0.2	0.48 ± 0.30	1.5	32.5 ± 24.9
And XXI	a	0.32 ± 0.11	4.18 ± 0.61	137.2 ± 9.7	0.54 ± 0.14	12.9	0.39 ± 0.12	0.1	0.44 ± 0.17	16.9	36.2 ± 10.8
And XXII	a	0.58 ± 0.14	1.14 ± 0.32	261.5 ± 33.6	0.77 ± 0.13	3.3	0.63 ± 0.13	0.0	0.72 ± 0.17	3.2	17.1 ± 8.6
And XXIII	a	0.38 ± 0.05	5.43 ± 0.40	130.3 ± 3.4	0.72 ± 0.07	57.4	0.40 ± 0.06	0.0	0.51 ± 0.14	16.1	35.3 ± 4.7
And XXIV	a	0.23 ± 0.15	2.92 ± 0.72	166.7 ± 24.8	0.30 ± 0.19	0.9	0.45 ± 0.24	2.9	0.38 ± 0.26	6.8	25.8 ± 13.4
And XXV	p	0.20 ± 0.11	3.18 ± 0.33	111.9 ± 32.2	0.33 ± 0.17	21.2	0.32 ± 0.17	1.3	0.31 ± 0.18	18.3	23.3 ± 14.0
And XXVI	p	0.30 ± 0.20	1.45 ± 0.49	197.6 ± 108.9	0.43 ± 0.27	2.7	0.54 ± 0.28	0.8	0.48 ± 0.29	2.1	20.6 ± 17.0
Cas II	p	0.38 ± 0.07	1.47 ± 0.14	176.2 ± 40.4	0.45 ± 0.09	0.3	0.69 ± 0.12	0.0	0.57 ± 0.21	1.1	36.1 ± 10.0
NGC 147	p	0.46 ± 0.02	6.70 ± 0.09	118.6 ± 10.1	0.63 ± 0.07	1.6	0.58 ± 0.06	0.0	0.60 ± 0.15	10.4	39.1 ± 4.8
NGC 185	p	0.22 ± 0.01	2.94 ± 0.04	181.9 ± 15.7	0.24 ± 0.01	0.0	0.60 ± 0.04	0.0	0.42 ± 0.23	1.2	24.8 ± 2.3

Note. *Note that these values are calculated according to the γ -deprojection tidal rejection criterion.

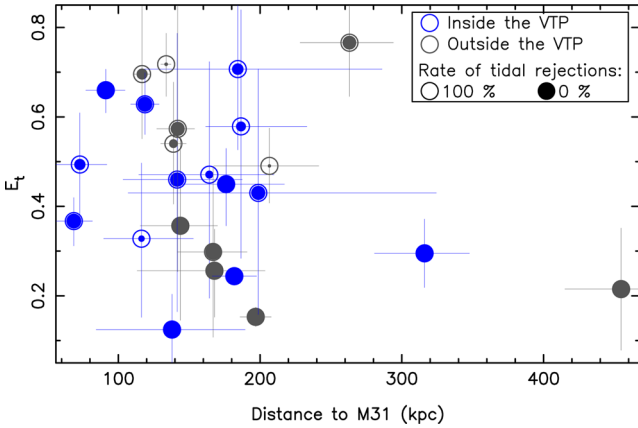


Figure 17. Tangentially deprojected ellipticity versus distance to Andromeda. Blue circles are the values for the satellites in the VTP of galaxies (Ibata et al. 2013), while grey circles are for the ones outside. The filling of these circles represents the tidal rejection rate (see labels in the top-right box).

Table 2. Average ellipticities of the whole sample of dwarf galaxies of Andromeda used in this work, obtained from 25×10^5 draws of the MCMC chain.

	Mean ellipticity	Tidally rejected (per cent)
ϵ	0.32 ± 0.11	–
E_t	0.44 ± 0.14	9.22
E_r	0.54 ± 0.15	4.12
E_γ	0.48 ± 0.21	9.14

be made of the same type of objects as also recently concluded by Collins et al. (2015). Nevertheless, we noted that the distribution of ellipticity versus distance to M31 in the tangential deprojection case was slightly different for galaxies inside and outside of the VTP.

REFERENCES

- Bahl H., Baumgardt H., 2014, *MNRAS*, 438, 2916
 Barber C., Starkenburg E., Navarro J. F., McConnachie A. W., 2015, *MNRAS*, 447, 1112
 Belokurov V. et al., 2006, *ApJ*, 647, L111
 Carraro G., 2014, preprint (arXiv:1406.1243)
 Collins M. L. M. et al., 2013, *ApJ*, 768, 172
 Collins M. L. M. et al., 2014, *ApJ*, 783, 7
 Collins M. L. M. et al., 2015, *ApJ*, 799, L13
 Conn A. R. et al., 2012, *ApJ*, 758, 11
 Crnojević D. et al., 2014, *MNRAS*, 445, 3862
 Famaey B., McGaugh S. S., 2012, *Living Rev. Relativ.*, 15, 10
 Fardal M. A. et al., 2013, *MNRAS*, 434, 2779
 Foot R., Silagadze Z. K., 2013, *Phys. Dark Universe*, 2, 163
 Freeman K., Bland-Hawthorn J., 2002, *ARA&A*, 40, 487
 Hammer F., Yang Y., Fouquet S., Pawlowski M. S., Kroupa P., Puech M., Flores H., Wang J., 2013, *MNRAS*, 431, 3543
 Ibata R. A. et al., 2013, *Nature*, 493, 62
 Ibata R. A. et al., 2014a, *ApJ*, 780, 128
 Ibata R. A., Ibata N. G., Lewis G. F., Martin N. F., Conn A., Elahi P., Arias V., Fernando N., 2014b, *ApJ*, 784, L6
 Klein C. R., Cenko S. B., Miller A. A., Norman D. J., Bloom J. S., 2014, preprint (arXiv:1405.1035)
 Kravtsov A. V., Gnedin O. Y., Klypin A. A., 2004, *ApJ*, 609, 482
 Kroupa P., 1997, *Nature*, 2, 139

- Kroupa P., Theis C., Boily C. M., 2005, *A&A*, 431, 517
 Kroupa P. et al., 2010, *A&A*, 523, A32
 Lokas E. L., Kazantzidis S., Klimentowski J., Mayer L., Callegari S., 2010, *ApJ*, 708, 1032
 McConnachie A. W., 2012, *AJ*, 144, 4
 McConnachie A. W. et al., 2008, *ApJ*, 688, 1009
 McConnachie A. W. et al., 2009, *Nature*, 461, 66
 Martin N. F., de Jong J. T. A., Rix H.-W., 2008, *ApJ*, 684, 1075
 Martin N. F. et al., 2009, *ApJ*, 705, 758
 Martin N. F. et al., 2013, *ApJ*, 779, L10
 Milgrom M., 1983, *ApJ*, 270, 365
 Moretti M. I. et al., 2014, *MNRAS*, 437, 2702
 Navarro J. F., Frenk C. S., White S. D. M., 1997, *ApJ*, 490, 493
 Pawlowski M. S., McGaugh S. S., 2014, *MNRAS*, 440, 908
 Pawlowski M. S., Kroupa P., de Boer K. S., 2011, *A&A*, 532, A118
 Pawlowski M. S., Pflamm-Altenburg J., Kroupa P., 2012, *MNRAS*, 423, 1109
 Pawlowski M. S. et al., 2014, *MNRAS*, 442, 2362
 Peñarrubia J., Kroupa P., Boily C. M., 2002, *MNRAS*, 333, 779
 Randall L., Scholtz J., 2014, preprint (arXiv:1412.1839)
 Shaya E. J., Tully R. B., 2013, *MNRAS*, 436, 2096
 Tollerud E. J., Boylan-Kolchin M., Bullock J. S., 2014, *MNRAS*, 440, 3511
 Tolstoy E., Hill V., Tosi M., 2009, *ARA&A*, 47, 371
 Vera-Ciro C. A., Sales L. V., Helmi A., Navarro J. F., 2014, *MNRAS*, 439, 2863
 Walker M. G., Mateo M., Olszewski E. W., Peñarrubia J., Wyn Evans N., Gilmore G., 2009, *ApJ*, 704, 1274
 Walsh S. M., Jerjen H., Willman B., 2007, *ApJ*, 662, L83
 Watkins L. L., Evans N. W., An J. H., 2010, *MNRAS*, 406, 264
 Yang Y., Hammer F., Fouquet S., Flores H., Puech M., Pawlowski M. S., Kroupa P., 2014, *MNRAS*, 442, 2419
 Zhao H., Famaey B., Lüghausen F., Kroupa P., 2013, *A&A*, 557, L3
 Zolotov A., Hogg D. W., Willman B., 2011, *ApJ*, 727, L14
 Zucker D. B. et al., 2006, *ApJ*, 643, L103

APPENDIX A: TANGENTIAL CASE

We seek the vector \mathbf{m} which has the same projection on the sky as the half-light radius \mathbf{r}_h . This means it has the same projected PA (see equation A3). At the same time, \mathbf{m} must be perpendicular to the direction \mathbf{r}_s , between M31 and the centre of the dSph (see equation A2). First of all, for a dSph, we define a local coordinate system ($\mathbf{los}, \mathbf{n}, \mathbf{e}$) centred on the galaxy where the line-of-sight \mathbf{los} is one of the axes and where \mathbf{n} points towards the north. From (standard) sky coordinates (χ, η) with respect to the centre, we obtain the local base:

$$\mathbf{los} = \begin{pmatrix} \cos \eta \sin \chi \\ \sin \eta \\ \cos \eta \cos \chi \end{pmatrix}, \mathbf{n} = \begin{pmatrix} -\sin \chi \sin \eta \\ \cos \eta \\ -\cos \chi \sin \eta \end{pmatrix}, \mathbf{e} = \begin{pmatrix} \cos \chi \\ 0 \\ -\sin \chi \end{pmatrix}. \quad (\text{A1})$$

From this base with our conditions and the normalization of \mathbf{m} , a three-equation system can be deduced:

$$\mathbf{r}_s \cdot \mathbf{m} = 0 \quad (\text{A2})$$

$$\tan(PA) = \frac{\mathbf{m} \cdot \mathbf{e}}{\mathbf{m} \cdot \mathbf{n}} \quad (\text{A3})$$

$$m_x^2 + m_y^2 + m_z^2 = 1. \quad (\text{A4})$$

The solution of this system gives us

$$\mathbf{m} = \begin{pmatrix} \frac{-1}{r_{sx} \sqrt{C}} \left(\frac{A r_{sy}}{B} + r_{sz} \right) \\ \frac{A}{B \sqrt{C}} \\ \frac{1}{\sqrt{C}} \end{pmatrix}, \quad (\text{A5})$$

where

$$\begin{cases} A = \tan(PA) \cos \chi \sin \eta r_{s_x} - \tan(PA) r_{s_z} \sin \chi \sin \eta \\ \quad - r_{s_z} \cos \chi - r_{s_x} \sin \chi \\ B = \tan(PA) r_{s_y} \sin \chi \sin \eta + r_{s_x} \tan(PA) \cos \eta \\ \quad + r_{s_y} \cos \chi \\ C = \frac{1}{r_{s_x}^2} \left(\frac{A r_{s_y}}{B} + r_{s_z} \right)^2 + \left(\frac{A}{B} \right)^2 + 1 \end{cases}$$

As we know \mathbf{m} , the norm of the tangentially deprojected semimajor axis b_t has yet to be discovered. DSph are considered as prolate (see equation A6). Thus, we are putting ourselves this time in the plane defined by \mathbf{los} and \mathbf{m} . The new local base (\mathbf{y}, \mathbf{z}) corresponds to the minor (a) and the semimajor axis (b_t) of the real prolate:

$$\frac{y^2}{a^2} + \frac{z^2}{b_t^2} = 1. \quad (\text{A6})$$

For the present purposes, dSph around M31 are far enough to be considered as being at infinity. Consequently, r_h is approximately seen between two parallel rays, \mathbf{los} and \mathbf{los}' with a separation of ω . We called α the angle between \mathbf{y} and \mathbf{los} . y_0 is the point at the intersection between \mathbf{y} and \mathbf{los}' . It follows that:

$$\sin \alpha = \frac{\omega}{y_0}. \quad (\text{A7})$$

From equation (A6), we obtain y and

$$\frac{dy}{dz} = \frac{-az}{b_t^2 \sqrt{1 - \frac{z^2}{b_t^2}}}. \quad (\text{A8})$$

With equation (A8), we obtain the equation for the straight line (d) which has \mathbf{los}' for guiding vector:

$$y = y_0 - \frac{az^2}{b_t^2 \sqrt{1 - \frac{z^2}{b_t^2}}}. \quad (\text{A9})$$

And so, the intersection between (d) (equation A9) and the prolate (equation A6) with equation (A7) gives

$$a = \frac{\omega}{\sin \alpha} \sqrt{1 - \frac{z^2}{b_t^2}}. \quad (\text{A10})$$

The development of equation (A11) with $\tan \alpha = -y'$ and $\beta_t = \frac{\pi}{2} - \alpha$ gives the final real semimajor axis, tangentially deprojected:

$$b_t = \sqrt{\left(\frac{\omega}{\sin \beta_t} \right)^2 - \left(\frac{a}{\tan \beta_t} \right)^2}. \quad (\text{A11})$$

APPENDIX B: RADIAL CASE

We seek the vector \mathbf{q} which has the same projection on the sky as the half-light radius \mathbf{r}_h . It means the same projected PA. At the same time, \mathbf{q} must be as close as possible to the radial direction \mathbf{r}_s , connecting M31 with the centre of the dSph (see equation A2). We place the system in the same basis as the tangential deprojection (see appendix A). The line of sight is again \mathbf{los} and \mathbf{m} is the tangential direction. Thus, \mathbf{q} must be placed in the plane \mathcal{P} defined by these two vectors. \mathcal{P} has as its normal vector $\mathbf{n}_{\mathcal{P}}$:

$$\mathbf{n}_{\mathcal{P}} = \begin{pmatrix} B n_{\mathcal{P}_z} \\ A n_{\mathcal{P}_z} \\ \frac{1}{\sqrt{1+A^2+B^2}} \end{pmatrix} \quad (\text{B1})$$

where

$$\begin{cases} A = \frac{r_x m_z - m_x r_z}{-r_x m_y + m_x r_y} \\ B = \frac{-m_y}{m_x} A - \frac{m_z}{m_x} \end{cases}$$

And so, with the minimum angle between \mathbf{q} and \mathbf{r}_s , the constraint of lying in Plane \mathcal{P} and the normalization of \mathbf{q} , a system of three equations can be deduced:

$$\begin{cases} \mathbf{q} \cdot \mathbf{n}_{\mathcal{P}} = 0 \\ \mathbf{q} \cdot \mathbf{r}_s = \max. \\ q_x^2 + q_y^2 + q_z^2 = 1 \end{cases} \quad (\text{B2})$$

This system is solved by maximizing equation B2:

$$\mathbf{q} = \begin{pmatrix} \frac{-1}{n_{\mathcal{P}_x}} (n_{\mathcal{P}_x} q_y + n_{\mathcal{P}_z} q_z) \\ \frac{-4n_{\mathcal{P}_y} n_{\mathcal{P}_z}}{n_{\mathcal{P}_y}^2 + n_{\mathcal{P}_x}^2} q_z \\ \frac{A \sqrt{1 - n_{\mathcal{P}_z}^2}}{\sqrt{A^2 + B^2}} \end{pmatrix} \quad (\text{B3})$$

where

$$\begin{cases} A = r_{s_z} \left((n_{\mathcal{P}_x}^2 + n_{\mathcal{P}_y}^2) - n_{\mathcal{P}_y} n_{\mathcal{P}_z} \right) - r_{s_x} n_{\mathcal{P}_z} n_{\mathcal{P}_x} \\ B = n_{\mathcal{P}_x} r_{s_y} - n_{\mathcal{P}_y} r_{s_x} \end{cases}$$

Finding the norm b_r follows the same approach as that for the tangential case and so

$$b_r = \sqrt{\left(\frac{\omega}{\sin \beta_r} \right)^2 - \left(\frac{a}{\tan \beta_r} \right)^2}. \quad (\text{B4})$$

This paper has been typeset from a $\text{\TeX}/\text{\LaTeX}$ file prepared by the author.